Suppression of epitaxial grain growth in laser powder bed fusion fabricated Inconel 625 through intermittent variation of the build layer thickness

Jie Zhu a), Jintao Xu a), Hiroyuki Kokawa a, c), Yakai Zhao d, e), Kai Feng a, b) *, Zhuguo Li a, b)*, Upadrasta Ramamurty d, e)

a) Shanghai Key Laboratory of Materials Laser Processing and Modification, School of Materials Science and Engineering, Shanghai Jiao Tong University, Shanghai, 200240, China

b) Collaborative Innovation Center for Advanced Ship and Deep-Sea Exploration, Shanghai, 200240, China

c) Department of Materials Processing, Tohoku University, Sendai 980-8579, Japan

d) School of Mechanical and Aerospace Engineering, Nanyang Technological University, Singapore 639798, Republic of Singapore

e) Institute of Materials Research and Engineering, Agency for Science, Technology and Research, Singapore 138634, Republic of Singapore

*Corresponding Authors:

E-mail address: fengkai@sjtu.edu.cn (Kai Feng).

E-mail address: lizg@sjtu.edu.cn (Zhuguo Li).

Abstract

Microstructural anisotropy, which often leads to anisotropy in the mechanical performance, induced by the epitaxial grain growth during solidification is a major concern in a number of metal and alloy components that are manufactured using the additive manufacturing technique of laser powder bed fusion (LPBF). In this work, we demonstrate that a periodic variation in the layer thickness during LPBF results in the alteration of the grain growth direction and can effectively suppress the formation of columnar grains. Such a build strategy simultaneously decreases the grain size and the texture intensity, resulting in a reduced anisotropy in the mechanical properties. The variation of grain growth direction can be rationalized by thermal gradient variation near the transition area that occurs after the layer thickness is altered. This simple strategy provides an additional and new tool for grain structure tailoring during LPBF.

Keywords： Laser powder bed fusion; Nickel alloys; Layer thickness variation; Epitaxial growth; Anisotropy.

1. Introduction

Columnar microstructure—often oriented along the build direction (BD) and a result of the epitaxial grain growth—is a common feature in many alloys that are additively manufactured (AM) using techniques such as the laser powder bed fusion (LPBF)[1-6]. While such a microstructure is desirable in some contexts (AM of directionally solidified superalloys[7], for example), it (or those with a strong texture) is often deemed a major issue that must be overcome, due to the mechanical anisotropy it might induce[8, 9].

Two approaches are widely employed to 'break' the long columnar grains and realize an equiaxed microstructure with a random texture. First is the addition of inoculants or solutes to the alloy powder [4, 10-13]. Such additions either create heterogenous nucleation sites ahead of the solidification front or facilitate the constitutional undercooling [12]. Both these mechanisms could result in a microstructure with fine equiaxed grains. While this is indeed a good and practical method, it would not only require the reevaluation of the powder production methodology, but also alter the constituent phases and hence the structural reliability, corrosion resistance, and/or other properties of the fabricated parts.

The second approach for breaking the columnar grain structure is to adapt a processing parameter combination that prevents the formation of such grains. The underlaying principle in this approach involves the balancing of the thermal gradient (*G*) and the solidification rate (*R*) to manipulate the solidification mode or direction to realize the desirable grain structure. Prior studies have shown that this approach for realizing the columnar-to-equiaxed transition (CET) may not always be cost effective within the process parameter window available for LPBF[14]. The research performed thus far indicates that the interplay between the melt pool geometry[15], crystallographic texture of the substrate plates used for LPBF[16], and the variation in *G* are the keys to the grain structure control during LPBF[17]. Towards this end, manipulation of the laser spot size[18], the laser power and scan speed combination [19-23], large hatch spacing[24-26], scanning strategy optimization[27-29], and altering the profile of the laser beam [17, 30] were all shown to be effective in the grain structure control. Nevertheless, these methods involve complicated re-optimization of the process parameters or even redevelopment of the LPBF machine in some contexts. Keeping this in mind, we demonstrate here a simple methodology to control the grain structure in the LPBF Inconel 625 (IN625) – an extensively studied Ni-based superalloy produced using LPBF. Significant mechanical anisotropy in it, processed using many different LPBF machines with different parameters, were reported[31-33]. By tailoring the layer thickness variation (LTV) during LPBF—but without changing other process parameters or scanning strategy—the epitaxial growth of columnar grains is circumvented.

2. Experimental details

2.1 Fabrication of specimens

Commercially available gas-atomized IN625 powder (diameters in the range of ~15–53 μm) were utilized for LPBF by using an HBD-80 machine with the following build parameters: laser power 175 W, laser scan speed 800 mm/s, hatch spacing 0.11

mm, where laser travels bidirectionally during building process. The specimens for the microstructural analyses were fabricated with the dimensions of 1.8 mm (thickness/height) × 6 mm (width) × 6 mm (length).

Figures 1 (a), (b), (f), and (g) show the schematic illustrations of the specimens with either 0.02 or 0.03 mm layer thickness (LT) (all the other process parameters being identical) with either 0° or 67° interlayer rotation. These specimens are labelled as LT2-0, LT3-0, LT2-67, and LT3-67 depending on the layer thickness (LT) and interlayer rotation angle. Here, ‘0’ and ‘67’refer to the interlayer rotations of 0° and 67°, respectively; in the former, the laser traversed bidirectionally along the X direction. These two scanning strategies were adopted since they are the most commonly used ones in different LPBF machines[33]. The 0° scanning strategy was utilized since the 0-XOY, 0-XOZ and 0-YOZ planes of the specimens built with this strategy would reflect the distinct features of the microstructures along different directions. The 67° scan rotation between successive layers, on the other hand, was adopted to verify the influence of LTV strategy, since this is the most widely used scan strategy. The numbers ‘2’ and ‘3’ that follow LT refer to the layer thicknesses used: 0.02 and 0.03 mm, respectively.

In the LTV specimens, LT was varied, as illustrated in Figs. 1 (c) and (d). In these specimens, the first 0.3 mm thick material was removed (subsequent to the fabrication of the coupons) to eliminate any potential influence of the substrate’s texture on the built part’s microstructure[34]. Several different LT combinations (listed in Table 1) were utilized to build the rest of the 1.8 mm of the coupons. To make sure each segment can be divided evenly by both the 0.02 and 0.03 mm LTs, the thickness of the segment was selected to be either 0.9 or 0.6 mm for different LTV strategies. The densities of specimens were not affected due to LTV, and near fully dense specimens were always obtained, as demonstrated from the optical microscopy (OM) images displayed in Fig. S1 of the supplementary material.

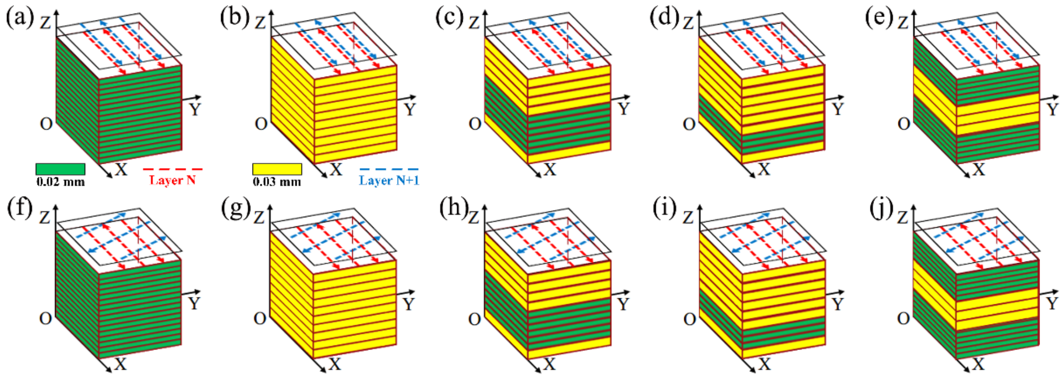

Fig. 1 (a) - (e) Schematic illustrations of the LT2-0, LT3-0, LT23-0, LT233-0, and LT232-0 specimens. (f) - (j) Schematic illustrations of the LT2-67, LT3-67, LT23-67, LT233-67, and LT232-67 specimens. Here, the green and yellow colors represent segments that are built by using 0.02 mm and 0.03 mm layer thicknesses, respectively.

Table 1. Layer thickness variation strategy of LTV specimens

Specimen (total height = 1.8 mm)	**Height of each segment**	**Building layer thickness in each part (bottom to top)**
LT23	0.9 mm	0.02 mm — 0.03 mm
LT233	0.6 mm	0.02 mm — 0.03 mm — 0.03 mm
LT232	0.6 mm	0.02 mm — 0.03 mm — 0.02 mm

Additionally, dog-bone specimens for tensile testing were also directly fabricated using LPBF, as illustrated in Fig. 2. The gauge dimensions of the dog-bone specimens are 2.1 mm (thickness) × 4 mm (width) × 15 mm (length) while the total length of the tensile specimen is 60 mm. Two types of tensile specimens labelled as VER (in which the loading axis is parallel to the build direction (BD)), and HOR (in which the loading axis is perpendicular to BD) were manufactured. Specimens were cut from the substrate plates by using the wire electrical discharge machining (WEDM). For the VER specimens, the printing pattern follows those shown in Fig. 1 and Table 1, since the 2.1 mm thickness matches those for microstructural observations (1.8 mm) plus the initial 0.3 mm. The HOR specimens, on the other hand, were printed such that the patterns shown in Fig. 1 and Table 1 were repeated periodically throughout the total print height (60 mm). To verify the potential influence of the height difference between HOR and VER specimens on the cooling rate and hence the microstructure and mechanical properties, additional blocks were built to the same height as VER sample (60 mm), wherein ‘HOR specimens’ (2.1 mm thick) were extracted by WEDM, as schematically illustrated in Fig. 2. Experimental results show that the mechanical property data obtained on these specimens is consistent with that obtained on the HOR specimens, implying that the printing height does not result in any obvious deviation. Thus, only HOR and VER samples are compared in this study.

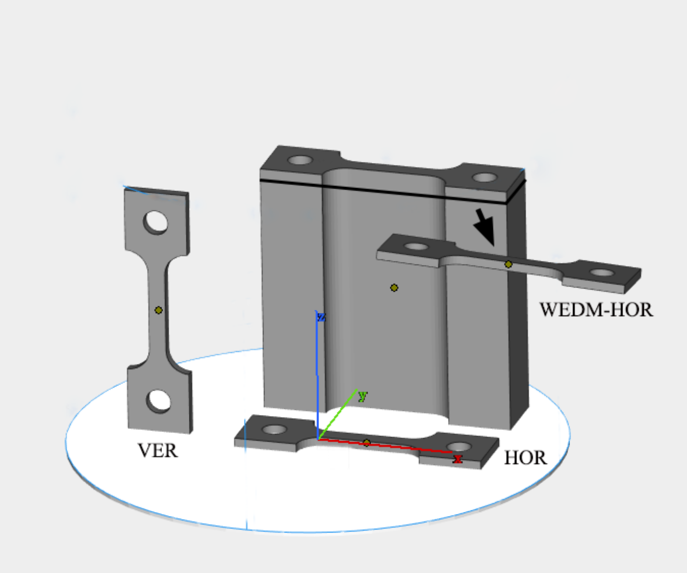

Fig. 2 Illustration of tensile specimens.

2.2 Microstructural characterization and mechanial tests

Due to the unique microstructures of the LTV specimens, all the specimens were cut into equal size (3 mm × 3 mm × 1.8mm) and the observations on the LTV specimens was always performed in the center of different observed planes, so as to properly reflect their representative microstructures.

For OM using a Zeiss Axio Imager A2m, specimens were ground and mechanically polished using 1 μm diamond suspension. For electron back scattered diffraction (EBSD) characterizations with a Nova NanoSEM 230 equipped with an Oxford detector, specimens were further vibration polished. Electron backscattered diffraction (EBSD) was performed at a step size of 3 μm, and the data were analyzed using the commercial AZtec Crystal Software.

Before mechanical testing, the gauge parts of the tensile specimens were ground using sandpapers till grit number of 1200 to ensure flat surfaces. Tensile tests were performed using a Z020 THW tensile machine (equipped with a contact extensometer) at room temperature at a nominal strain rate of 10^{-3} /s. For each condition, three repeat tests were conducted.

3. Results and discussion

3.1 LTV specimens with 0° interlayer rotation

Figure 3 shows the inverse pole figure (IPF) maps with corresponding grain boundary (GB) maps of different specimens. Both the LT2-0 and LT3-0 specimens show similar microstructural features. In the XOY plane, the microstructure reflects the laser scanning strategy adapted along the X direction and is similar to that reported in many studies that utilized a similar strategy[23, 35]. The grains on the XOZ planes of both the specimens exhibit columnar features since no interlayer rotation was applied to prevent the epitaxial grain growth. The microstructures on the YOZ planes exhibits a mix of columnar and stray fine grains.

The microstructures of 0.02 mm layer-thickness segment (referred to as 'LT2 segment' hereafter), colored green in Figure 3, in the LT23-0, LT233-0, and LT232-0 specimens are similar to that seen in the LT2-0 specimen. The grains in the 0.03 mm layer-thickness segment after LTV ('LTV3 segment', or the yellow regions), on the contrary, are refined compared to those in the LT3-0 specimen, which is especially prominent on the XOZ plane. Pole figures obtained on the XOZ planes of different specimens are displayed in Fig. 3 (f) to (j). Texture analyses of data obtained on the LT2 and LT3 specimens shows that the <001> directions tend to align with building direction, with the maximum intensity being 10.42 and 8.55 times the random orientation distribution, respectively. In the LTV specimens, however, a significant decrease of the <001> texture intensity is noted. The maximum intensities decreased to 8.31 in the LT23-0 specimen, 7.81 in the LT233-0 specimen, and 5.7 in the LT232-0 specimen. Moreover, a less intense <110> texture can be observed in the {110} pole figures as well, indicating a possible deflection in the grain growth direction after the application of the LTV strategy. These features indicate a positive effect of LTV strategy in breaking the growth of columnar grains and thus promoting a more isotropic microstructure. However, it appears that the grain refinement only occurs at the transition regions of the LT2 to LTV3 segments (green to yellow grains in Figures 3 (c)–(e)). Growth of columnar grains tends to reappear after the transition of the LT3 to LTV2 segment (yellow to green grains in Figure 3 (e)).

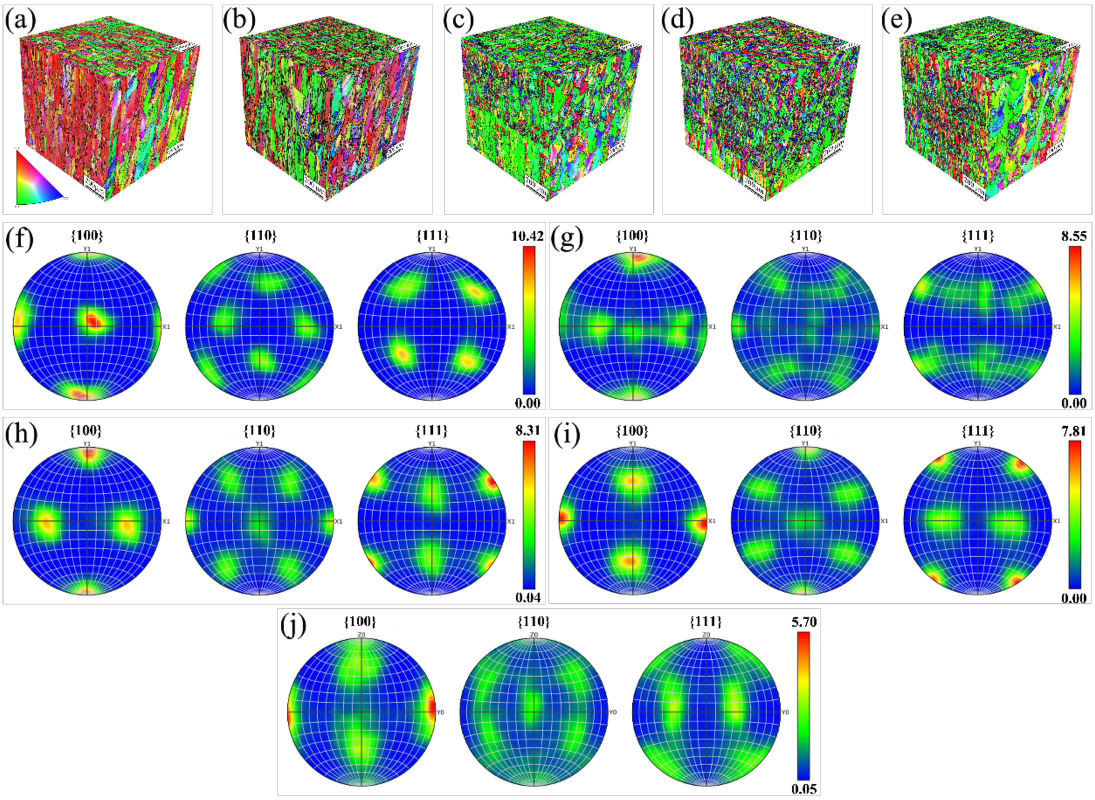

Fig. 3 (a) – (e) IPF-GB maps of the LT2-0, LT3-0, LT23-0, LT233-0, and LT232-0 specimens (all the planes observed along building direction) and (f) – (j) pole figures of their XOZ planes.

For a quantitative evaluation of the changes to the grain size, *d*, the area-weighted average grain size, $\overline{d_a}$, was utilized. This was done so as to reduce the statistical errors caused by the differences in the number of columnar and fine grains when considering the arithmetic average of d.[9] The values of $\overline{d_a}$ in different parts of the LT23-0 and LT233-0 specimens were estimated by using the relation: $\overline{d_{aw}} = \sum_{1}^{N} \frac{d_i S_i}{S}$, where N is the number of grains considered, d_i is the equivalent diameter of the grain, S_i is the area of the grain, and S is the total area of all the grains considered. Typically, the grains on the XOY planes (sometimes called 'top surface' in the literature) of the LPBF alloys show insignificant anisotropy in their morphology[36], which is also the case here (as seen from Fig. 4). Hence, the variations in $\overline{d_a}$ on XOY planes were not considered here after. Variations in $\overline{d_a}$ in the LT2 and LTV3 segments of the LT23-0 and LT233-0 samples are displayed in Fig. 4 (a). The relative reduction in $\overline{d_a}$, δ ($= \frac{\overline{d_{aw-LT2}} - \overline{d_{aw-LTV3}}}{\overline{d_{aw-LT2}}}$) is also shown in the same figure, while the distributions in *d* are shown in Figures 4 (b) to (e). A significant reduction in $\overline{d_a}$ in the LTV3 segment, especially on XOZ planes, can be noted. In addition, as shown in Figures 4 (b) to (e), the fraction of large grains also decreased which results in a more uniform grain size distribution overall.

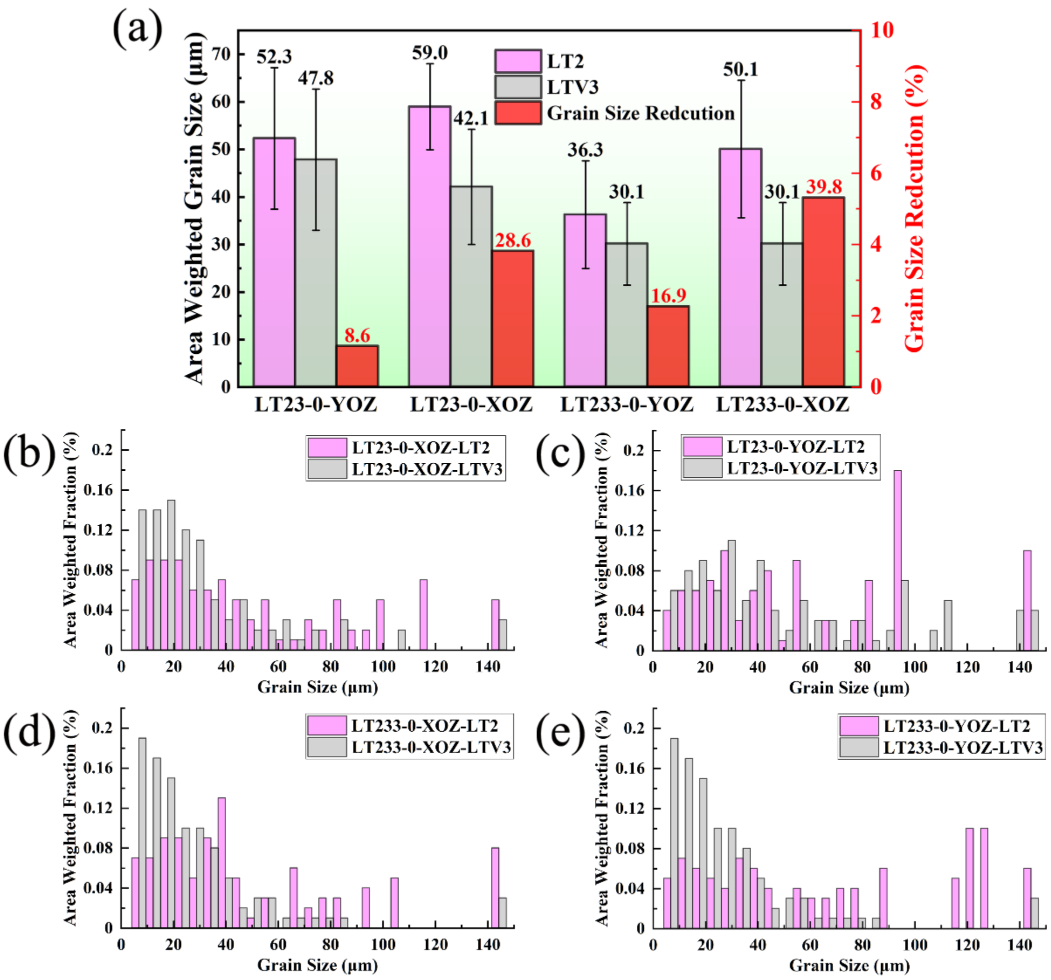

Fig. 4 (a) Area weighted grain size and grain size reduction of the specimens. (b) – (e) Grain size distribution of the LT23-0-XOZ, LT23-0-YOZ, LT233-0-XOZ and LT233-0-YOZ specimens, respectively.

3.2 LTV specimens with 67° interlayer rotation

The above results confirm that LTV from 0.02 to 0.03 mm during LPBF is effective in reducing the grains size as well as its anisotropy when a bidirectional printing strategy (0° interlayer rotation) is utilized. To further explore the influence of LTV strategy on the grain structure in a more realistic situation, the effect of most widely used 67° interlayer rotation was also explored. For this purpose, LT2-67, LT3-67, LT23-67, and LT233-67 specimens were fabricated and analyzed. Both the VER and HOR tensile specimens were manufactured and tested. The LT232-67 specimen was not investigated here due to the insignificant improvement in the isotropy of grain structure in LT232-0.

Microstructural analyses of the LT2-67, LT3-67, LT23-67, and LT233-67 specimens (see Figs. 6 (a)–(d)) shows that the reduction in $\overline{d_a}$ in the LTV3 segments is similar to that noted in the LT23-0 and LT233-0 (Fig. 4 (a)) specimens. Notably, $\overline{d_a}$ reduced ~30% in XOZ and YOZ planes of both the LTV specimens. Besides, a uniform grain size distribution can be noted, as shown in Figures 6 (b) to (e). It was accompanied by a reduction in the crystallographic texture intensity as well, as illustrated through the pole figures obtained on the XOZ planes in Figs. 5 (g) and (h). (Pole figures of the YOZ plane were not shown here because of the similar microstructural features of the XOZ and YOZ planes when built with the 67° interlayer rotation.) In the LT2-67 and LT3-67 specimens, <001> texture along the building direction can still be observed in the {100} pole figures, indicating limited effect of interlayer rotation on reducing the anisotropy of microstructure. In the specimens built using LTV strategy, on the other hand, no obvious texture is seen. The maximum texture intensities are 2.39 and 2.45 in the LT23-67 and LT233-67 respectively, suggesting a prominent effect of LTV strategy on reducing the anisotropy of microstructure.

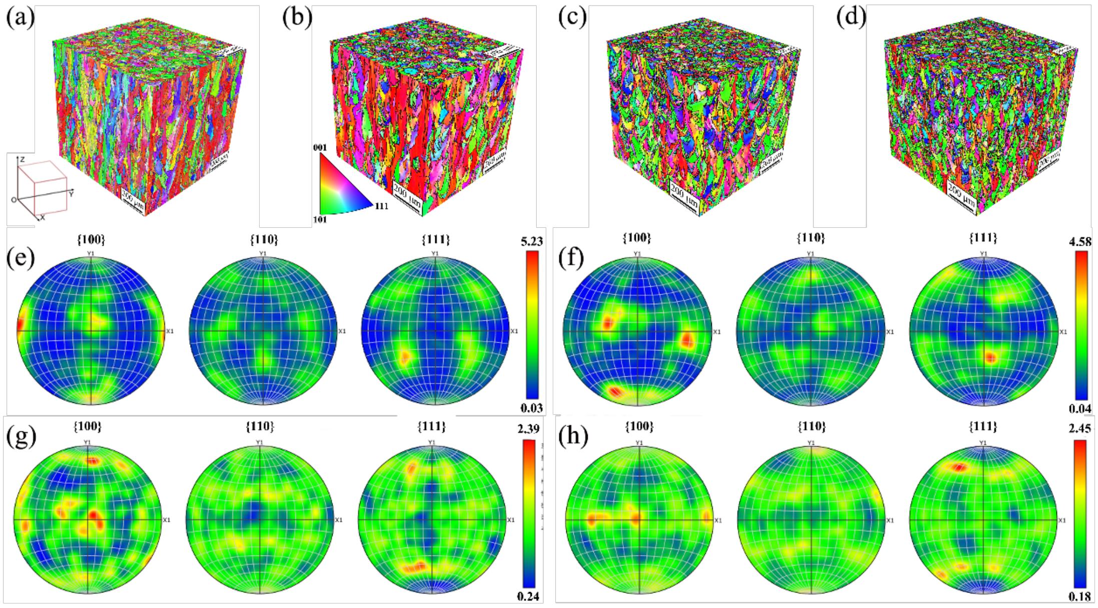

Fig. 5. (a)–(d) IPF-GB maps of LT2-67, LT3-67, LT23-67, and LT233-67 specimens, respectively. (The IPF maps are all along the building direction). (e)–(h) Pole figures of XOZ planes of LT2-67, LT3-67, LT23-67, and LT233-67, respectively

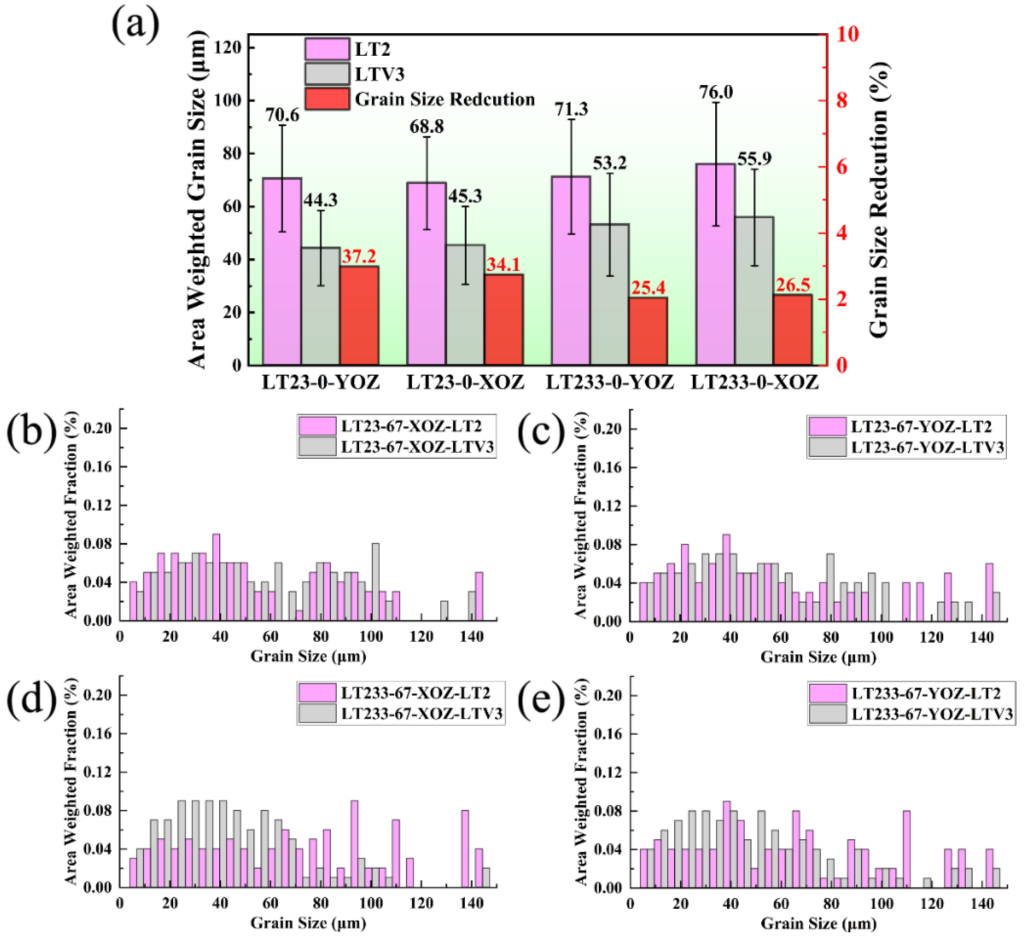

Fig. 6 (a) Area weighted grain size and grain size reduction of the specimens. (b) – (e) Grain size distribution of the LT23-67-XOZ, LT23-67-YOZ, LT233-67-XOZ, and LT233-67-YOZ, respectively.

For the LTV specimens, such as LT23-67 and LT233-67, columnar grains still exist in their LT2 segments, but with further optimization of the LTV strategy, isotropic microstructure and mechanical properties can be expected. Such a weakening of texture intensity helps in reducing the anisotropy in the tensile properties. Fig. 7 shows the representative tensile stress-strain responses and the mechanical properties extracted from such responses obtained on different specimens. It is noted from Fig. 7 (a) that the degree of anisotropy in the yield strength $\left(\Delta= \frac{\overline{\sigma_{S-HOR}}-\overline{\sigma_{S-VER}}}{\overline{\sigma_{S-HOR}}}\right)$ decreased from 20.7% in LT2-67 and 15.3% in LT3-67 to 13.7% in LT23-67 and 10.7% in LT233-67. The anisotropy degree in the ultimate tensile strength decreased slightly as well, as shown in Fig. 7 (c). A marginal reduction in the elongation to failure of the LTV-HOR specimens (from ~35% in LT2-67 and LT3-67 to ~30% in LT23-67 and LT233-67) was also noted. This mild reduction in elongation might have been a result of the strain incompatibility between the LT2 and LTV3 segments caused by the difference in their grain structures.

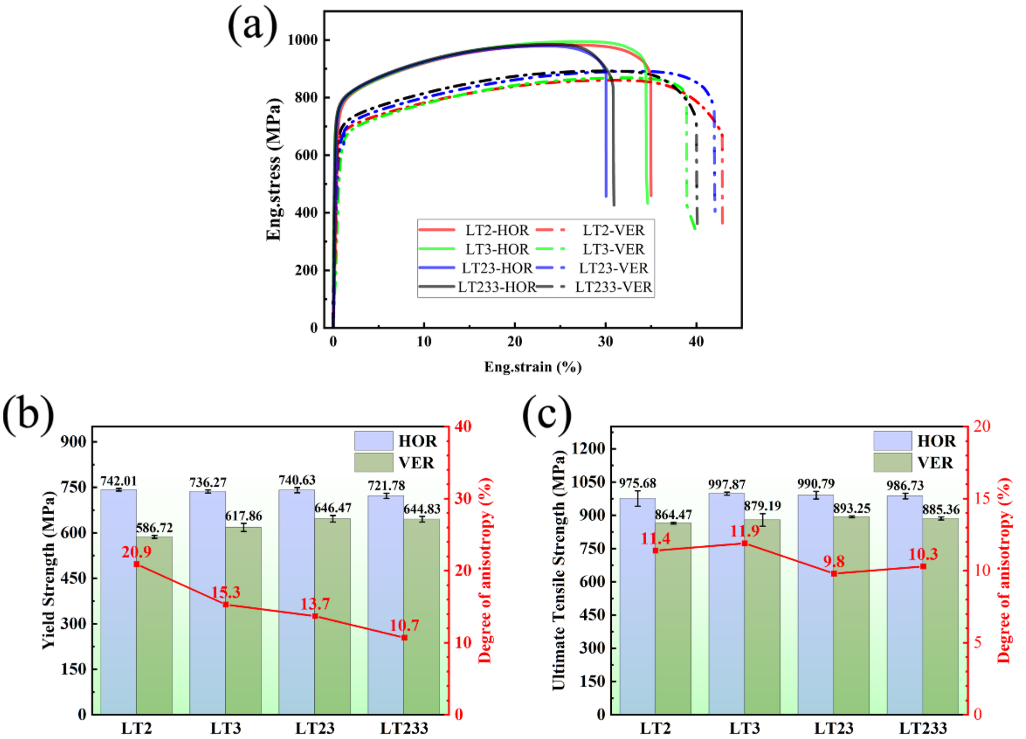

Fig. 7 (a) Representative tensile curves of LT2-67, LT3-67, LT23-67, LT233-67 specimens along horizontal and vertical direction and (b) and (c) their corresponding yield strength, ultimate tensile strength, and degree of anisotropy of mechanical properties.

3.3 Microstructural evolution near trasition area

To investigate the reasons responsible for the observed decrease in the grain size and the variations in the crystallographic texture after LTV, additional LPBF experiments were conducted such that only three 0.03 mm layers were printed on the LT2-0 specimen. Grain structure evolutions near the transition area of LTV on the XOZ and YOZ planes were studied, and the results are displayed in Fig. 8. The melt pool geometry in the YOZ plane of LTV3 (Fig. 8 (b)) remained the same as that of LT3-0 (Fig. 8 (a)). This observation suggests that LTV had no effect on the melt pool geometry, which would otherwise have influenced the epitaxial growth of grains. As shown in Figs. 8 (b-I), fine grains formed in the overlapping area of two neighboring melt pools in LTV3. Results of the detailed EBSD mapping on this area are presented in Fig. 8 (b-

II). While the grains labeled 1 and 4 maintained the epitaxy beyond the melt pool boundaries, grain 2 formed as a result of the competitive growth of the neighboring melt pools; grains 3, 5, and 6 did not grow epitaxially to 'follow' the crystallographic orientation of grain 2. The crystallographic orientation of grain 3 was slightly tilted towards BD, compared to that of grain 2, indicating a tendency of grain growth along the thermal gradient, G_z, that exists along BD. Compared to grain 3, crystallographic orientations of grains 5 and 6 turned towards the center of melt pool, which seems to be a result of grain growth affected by the increase in the transverse thermal gradient (Gy). The variation of thermal gradient at the bottom of melting pool is no doubt related to the increase in the layer thickness.

The grain structure on the XOZ plane of the LTV3 (Figs. 8 (d) and (d-II)) corresponds to that on the YOZ plane (Figs. 8 (b) and (b-II)) due to the 90º rotation around Z axis. Detailed analyses of the positional relationships, displayed in Figs. 8 (b), (b-I), (d), and (d-II), reveal that the grains labeled A, B, C, and D on the XOZ plane correspond to grains 1, 2, 5, and 6 on the YOZ plane, respectively. It should be noted that these grains are not exactly the same grains as discussed above on YOZ plane, but their positional relationships are similar such that the orientation variations are properly reflected. Differences in crystallographic grain orientations of these grains confirm the large variations of grain growth directions in the transition area. Besides, an increase of grain growth along longitudinal thermal gradient (G_x) is expected when considering the crystallographic orientation variations of the grains B, C, and D on the XOZ plane.

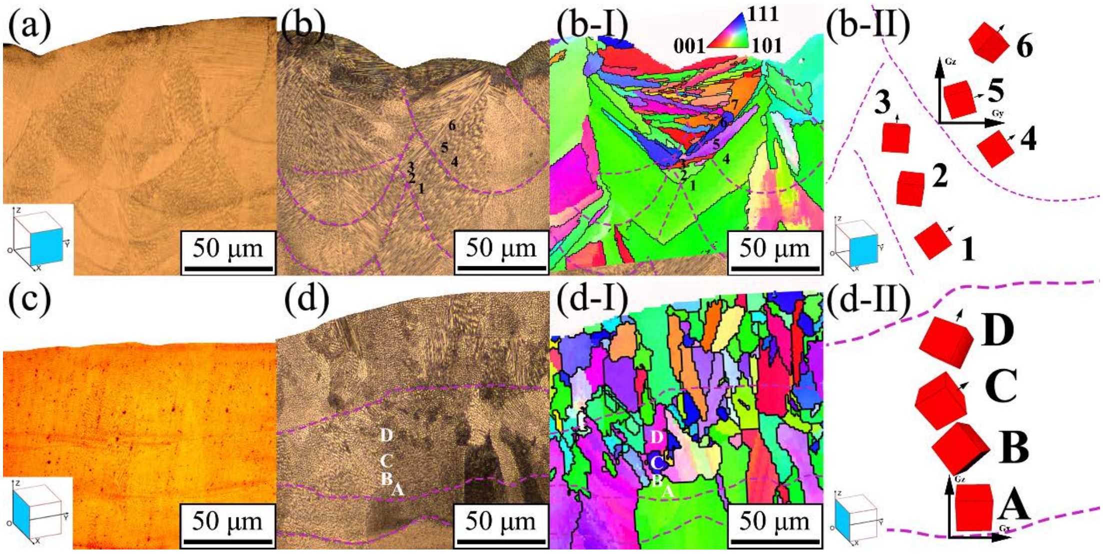

Fig. 8. (a) and (c) OM images of LT3-0 of YOZ and XOZ planes. (b) and (d) OM images of YOZ and XOZ planes of specimen with three layers of 0.03 mm layer thickness on the top of LT2-0. (b-I) and (b-II) IPF-GB maps (observed along building direction) and corresponding grain orientation of (b). (d-I) and (d-II) IPF-GB maps and corresponding grain orientation of (d).

In the above additional experiment, the printing process for each layer is the same as that used for fabricating the LT2 and LT3 specimens. Therefore, the same thermal gradients should exist for successive layers, thereby promoting the epitaxial growth of columnar grains, as illustrated schematically in Figs. 9 (a) and (b). This is the main reason for the anisotropic grain structure in the LPBF specimen, when built using an invariant LT. The color scheme used in Fig. 9 schematically represents different thermal gradients that exist during processing. While the lighter yellow color represents a milder thermal gradient, the darker red represents a steep one. With a similar melting pool geometry, a steeper thermal gradient at the bottom of melting pool can be expected when a smaller LT is used, i.e., LT2 (as represented by the red color in Fig. 9 (a) as compared to the orange color in LT3 in Fig. 9 (b))[37].

Through LTV with LT2 to LT3 transition, the thermal gradient near the LTV layers is altered (T_{31}, T_{32} and T_{33} in Fig. 9 (c)), whereas the melting pool geometry and crystallographic orientations (C_{31}, C_{32} and C_{33} in Fig. 9 (c)) of the substrate grains remain unchanged. This, in turn, results in an unfavorable condition for epitaxial growth of the grains in the LTV layer due to a relatively shallower thermal gradient (Fig. 9 (c)). Therefore, a simple thermal gradient variation can effectively change the growth direction (GD) of grains. In the subsequent LTV layers, the growth directions of the grains continue to change because the substrate grain's crystallographic orientation is no longer suitable for the epitaxial growth even under similar thermal gradient and melt pool geometry (Fig. 9 (d)). As a result of the competitive grain growth, a decrease of grain size and weakening of texture intensity occur and contribute to the reduced anisotropy in mechanical properties.

It is important to note here that LTV is not always applicable to suppress epitaxial growth, as observed in the case of transition from LT3 to LT2. In this case, a steeper thermal gradient introduced by a smaller LT brings about a tendency to promote epitaxial growth. Thus, when the transition from LT3 to LT2 happens during printing, epitaxial growth would still occur. In addition, the as-formed small grains in LTV3 layers would still be ‘consumed’ during the remelting induced by the laser scanning of the subsequent layer. Thus, continuous epitaxial growth is observed in the case of LT3 to LT2 transition in LT232-0 sample.

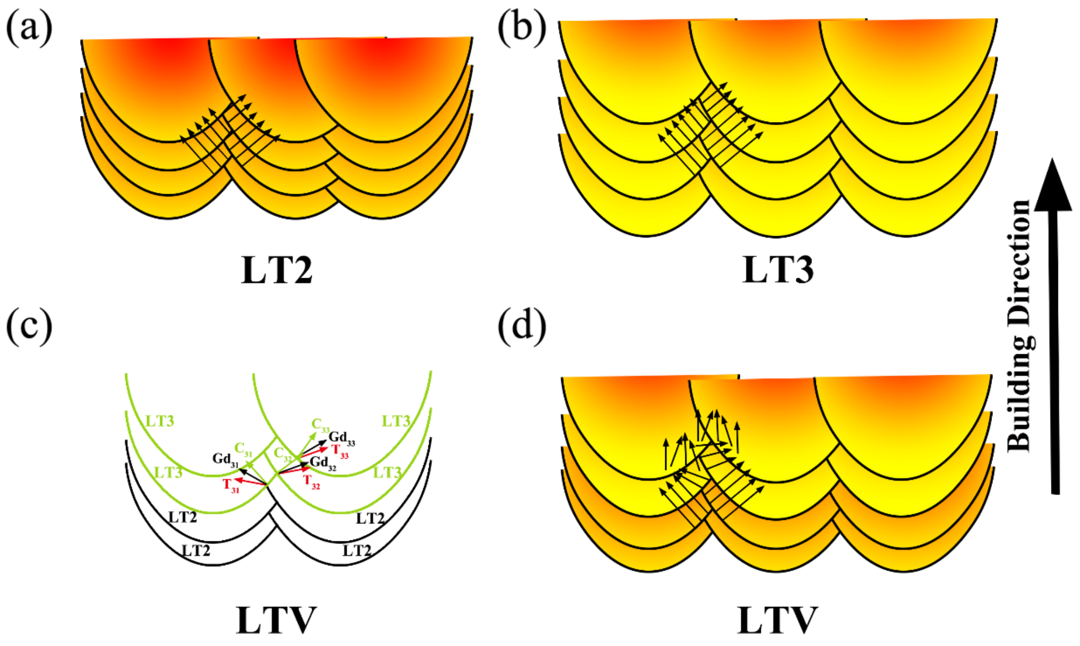

Fig. 9 Illustration of the grain growth in (a) LT2, (b) LT3 and LTV ((c) and (d)).

4. Conclusions

In summary, we have demonstrated that LTV during the LPBF of IN625 can effectively reduce the epitaxial growth of columnar grains and result in a significant decrease in grain size and weakening of the texture intensity. This LTV strategy can reduce the area-weighted grain size by ~30%, which is accompanied by a ~50% reduction of anisotropy in yield strength. A dispersion in the grain growth direction, caused by the thermal gradient variation, is the main reason for the suppression of the epitaxial growth near the transition area of LTV. This growth direction variation persisted in subsequently formed grains because the growth conditions are no longer suitable for epitaxial growth even though the thermal gradients are identical. This study provides a new strategy by combining and varying the relatively thick and thin LTs during LPBF for the microstructural manipulation as well as a potential improvement of productivity. This method could be a promising strategy that can be extended to many other alloys that are suitable to the LPBF process.

Acknowledgement

This work was financially supported by National Key R&D Program of China (No. 2022YFB4602102), Natural Science Foundation of Shanghai (Grant No.19ZR1425200). YZ and UR would like to thank the supports from Agency for Science, Technology and Research (A*STAR) of Singapore via the Structural Metal Alloys Programme (No. A18B1b0061). We would like to acknowledge the supports from Instrumental Analysis Center of Shanghai Jiao Tong University and Instrument and equipment sharing platform of School of Materials Science and Engineering, SJTU.

Data availability

The raw/processed data required to reproduce these findings cannot be shared at this time as the data also forms part of an ongoing study.

References

[1] B. Han, C. Zhang, K. Feng, Z. Li, X. Zhang, Y. Shen, X. Wang, H. Kokawa, R. Li, Z. Wang, P.K. Chu, Additively manufactured high strength and ductility CrCoNi medium entropy alloy with hierarchical microstructure, Mater. Sci. Eng., A, 820 (2021) 141545. https://doi.org/10.1016/j.msea.2021.141545.

[2] C. Zhang, K. Feng, H. Kokawa, B. Han, Z. Li, Cracking mechanism and mechanical properties of selective laser melted CoCrFeMnNi high entropy alloy using different scanning strategies, Mater. Sci. Eng., A, 789 (2020) 139672. https://doi.org/10.1016/j.msea.2020.139672.

[3] P. Kumar, U. Ramamurty, High cycle fatigue in selective laser melted Ti-6Al-4V, Acta Mater., 194 (2020) 305-320. https://doi.org/10.1016/j.actamat.2020.05.041.

[4] J.H. Martin, B.D. Yahata, J.M. Hundley, J.A. Mayer, T.A. Schaedler, T.M. Pollock, 3D printing of high-strength aluminium alloys, Nature, 549 (2017) 365-369. https://doi.org/10.1038/nature23894.

[5] J. Zhu, C. Shao, F. Lu, K. Feng, P. Liu, S. Chu, Y. Feng, H. Kokawa, Z. Li, Origin of the anisotropic ductility and the dynamic recrystallization-like deformation behavior of laser powder bed fusion Inconel 625 at elevated temperature, Scr. Mater., 221 (2022) 114945. https://doi.org/10.1016/j.scriptamat.2022.114945.

[6] Y.M. Wang, T. Voisin, J.T. McKeown, J. Ye, N.P. Calta, Z. Li, Z. Zeng, Y. Zhang, W. Chen, T.T. Roehling, R.T. Ott, M.K. Santala, P.J. Depond, M.J. Matthews, A.V. Hamza, T. Zhu, Additively manufactured hierarchical stainless steels with high strength and ductility, Nat Mater, 17 (2018) 63-71. https://doi.org/10.1038/nmat5021.

[7] X. Dang, Y. Li, K. Chen, U. Ramamurty, S. Luo, X. Liang, W. He, Avoiding cracks in additively manufactured non-weldable directionally solidified Ni-based superalloys, Addit. Manuf., 59 (2022) 103095. https://doi.org/10.1016/j.addma.2022.103095.

[8] T. DebRoy, H.L. Wei, J.S. Zuback, T. Mukherjee, J.W. Elmer, J.O. Milewski, A.M. Beese, A. Wilson-Heid, A. De, W. Zhang, Additive manufacturing of metallic components – Process, structure and properties, Prog. Mater Sci., 92 (2018) 112-224. https://doi.org/10.1016/j.pmatsci.2017.10.001.

[9] C. Zhang, K. Feng, H. Kokawa, Z. Li, Correlation between microstructural heterogeneity and anisotropy of mechanical properties of laser powder bed fused CoCrFeMnNi high entropy alloy, Mater. Sci. Eng., A, 855 (2022) 143920. https://doi.org/10.1016/j.msea.2022.143920.

[10] A. Prasad, L. Yuan, P. Lee, M. Patel, D. Qiu, M. Easton, D. StJohn, Towards understanding grain nucleation under Additive Manufacturing solidification conditions, Acta Mater., 195 (2020) 392-403. https://doi.org/10.1016/j.actamat.2020.05.012.

[11] Q. Tan, J. Zhang, Q. Sun, Z. Fan, G. Li, Y. Yin, Y. Liu, M.-X. Zhang, Inoculation treatment of an additively manufactured 2024 aluminium alloy with titanium nanoparticles, Acta Mater., 196 (2020) 1-16. https://doi.org/10.1016/j.actamat.2020.06.026.

[12] S. Wei, K.B. Lau, J.J. Lee, F. Wei, W.H. Teh, B. Zhang, C.C. Tan, P. Wang, U. Ramamurty, Selective laser melting of Fe–Al alloys with simultaneous gradients in composition and microstructure, Mater. Sci. Eng., A, 821 (2021) 141608. https://doi.org/10.1016/j.msea.2021.141608.

[13] S. Huang, R.L. Narayan, J.H.K. Tan, S.L. Sing, W.Y. Yeong, Resolving the porosity-unmelted inclusion dilemma during in-situ alloying of Ti34Nb via laser powder bed fusion, Acta Mater., 204 (2021) 116522. https://doi.org/10.1016/j.actamat.2020.116522.

[14] U. Scipioni Bertoli, B.E. MacDonald, J.M. Schoenung, Stability of cellular microstructure in laser powder bed fusion of 316L stainless steel, Mater. Sci. Eng., A, 739 (2019) 109-117. https://doi.org/10.1016/j.msea.2018.10.051.

[15] W. Liu, J.N. DuPont, Effects of melt-pool geometry on crystal growth and microstructure development in laser surface-melted superalloy single crystals: Mathematical modeling of single-crystal growth in a melt pool (part I), Acta Mater., 52 (2004) 4833-4847. https://doi.org/10.1016/j.actamat.2004.06.041.

[16] Z. Liu, H. Qi, Effects of substrate crystallographic orientations on crystal growth and microstructure formation in laser powder deposition of nickel-based superalloy, Acta Mater., 87 (2015) 248-258. https://doi.org/10.1016/j.actamat.2014.12.046.

[17] R. Shi, S.A. Khairallah, T.T. Roehling, T.W. Heo, J.T. McKeown, M.J. Matthews, Microstructural control in metal laser powder bed fusion additive manufacturing using laser beam shaping strategy, Acta Mater., 184 (2020) 284-305. https://doi.org/10.1016/j.actamat.2019.11.053.

[18] R. Jayaraj Radhakrishnan, P. Kumar, H.L. Seet, S.M.L. Nai, P. Wang, U. Ramamurty, Cascading of the as-built microstructure through heat treatment and its role on the tensile properties of laser powder bed fused Inconel 718, Materialia, 21 (2022) 101272. https://doi.org/10.1016/j.mtla.2021.101272.

[19] J. Liu, Y. Song, C. Chen, X. Wang, H. Li, C.a. Zhou, J. Wang, K. Guo, J. Sun, Effect of scanning speed on the microstructure and mechanical behavior of 316L stainless steel fabricated by selective laser melting, Mater. Des., 186 (2020) 108355. https://doi.org/10.1016/j.matdes.2019.108355.

[20] M. Liu, K. Wei, X. Zeng, High power laser powder bed fusion of AlSi10Mg alloy: Effect of layer thickness on defect, microstructure and mechanical property, Mater. Sci. Eng., A, 842 (2022) 143107. https://doi.org/10.1016/j.msea.2022.143107.

[21] H. Choo, K.-L. Sham, J. Bohling, A. Ngo, X. Xiao, Y. Ren, P.J. Depond, M.J. Matthews, E.

Garlea, Effect of laser power on defect, texture, and microstructure of a laser powder bed fusion processed 316L stainless steel, Mater. Des., 164 (2019) 107534. https://doi.org/10.1016/j.matdes.2018.12.006.

[22] H. Yang, L. Meng, S. Luo, Z. Wang, Microstructural evolution and mechanical performances of selective laser melting Inconel 718 from low to high laser power, J. Alloys Compd., 828 (2020) 154473. https://doi.org/10.1016/j.jallcom.2020.154473.

[23] S.-H. Sun, T. Ishimoto, K. Hagihara, Y. Tsutsumi, T. Hanawa, T. Nakano, Excellent mechanical and corrosion properties of austenitic stainless steel with a unique crystallographic lamellar microstructure via selective laser melting, Scr. Mater., 159 (2019) 89-93. https://doi.org/10.1016/j.scriptamat.2018.09.017.

[24] J. Pauza, A. Rollett, Simulation Study of Hatch Spacing and Layer Thickness Effects on Microstructure in Laser Powder Bed Fusion Additive Manufacturing using a Texture-Aware Solidification Potts Model, J. Mater. Eng. Perform., 30 (2021) 7007-7018. https://doi.org/10.1007/s11665-021-06110-7.

[25] N. Nadammal, S. Cabeza, T. Mishurova, T. Thiede, A. Kromm, C. Seyfert, L. Farahbod, C. Haberland, J.A. Schneider, P.D. Portella, G. Bruno, Effect of hatch length on the development of microstructure, texture and residual stresses in selective laser melted superalloy Inconel 718, Mater. Des., 134 (2017) 139-150. https://doi.org/10.1016/j.matdes.2017.08.049.

[26] M. Xia, D. Gu, G. Yu, D. Dai, H. Chen, Q. Shi, Influence of hatch spacing on heat and mass transfer, thermodynamics and laser processability during additive manufacturing of Inconel 718 alloy, Int. J. of Mach. Tools & Manuf., 109 (2016) 147-157. https://doi.org/10.1016/j.ijmachtools.2016.07.010.

[27] L.N. Carter, C. Martin, P.J. Withers, M.M. Attallah, The influence of the laser scan strategy on grain structure and cracking behaviour in SLM powder-bed fabricated nickel superalloy, J. Alloys Compd., 615 (2014) 338-347. https://doi.org/10.1016/j.jallcom.2014.06.172.

[28] Y.C. Wang, L.M. Lei, L. Shi, H.Y. Wan, F. Liang, G.P. Zhang, Scanning strategy dependent tensile properties of selective laser melted GH4169, Mater. Sci. Eng., A, 788 (2020) 139616. https://doi.org/10.1016/j.msea.2020.139616.

[29] K.A. Sofinowski, S. Raman, X. Wang, B. Gaskey, M. Seita, Layer-wise engineering of grain orientation (LEGO) in laser powder bed fusion of stainless steel 316L, Addit. Manuf., 38 (2021) 101809. https://doi.org/10.1016/j.addma.2020.101809.

[30] T.T. Roehling, R. Shi, S.A. Khairallah, J.D. Roehling, G.M. Guss, J.T. McKeown, M.J. Matthews, Controlling grain nucleation and morphology by laser beam shaping in metal additive manufacturing, Mater. Des., 195 (2020) 109071. https://doi.org/10.1016/j.matdes.2020.109071.

[31] A. Kreitcberg, V. Brailovski, S. Turenne, Effect of heat treatment and hot isostatic pressing on the microstructure and mechanical properties of Inconel 625 alloy processed by laser powder bed fusion, Mater. Sci. Eng., A, 689 (2017) 1-10. https://doi.org/10.1016/j.msea.2017.02.038.

[32] F. Zhang, Y. Luo, S. Yang, Y. Peng, T. Yang, J. Liu, Mechanical properties improvement of nickel-based alloy 625 fabricated by powder-fed laser additive manufacturing based on linear beam oscillation, Mater. Sci. Eng., A, 842 (2022) 143054. https://doi.org/10.1016/j.msea.2022.143054.

[33] C.U. Brown, G. Jacob, M. Stoudt, S. Moylan, J. Slotwinski, A. Donmez, Interlaboratory Study for Nickel Alloy 625 Made by Laser Powder Bed Fusion to Quantify Mechanical Property Variability, J. Mater. Eng. Perform., 25 (2016) 3390-3397. https://doi.org/10.1007/s11665-016-2169-2.

[34] C. Zhang, K. Feng, H. Kokawa, Z. Li, On the origin and evolution of cellular structures in

CoCrFeMnNi high entropy alloy fabricated by laser powder bed fusion, Mater. Charact., 196 (2023) 112586. https://doi.org/10.1016/j.matchar.2022.112586.

[35] O. Gokcekaya, T. Ishimoto, S. Hibino, J. Yasutomi, T. Narushima, T. Nakano, Unique crystallographic texture formation in Inconel 718 by laser powder bed fusion and its effect on mechanical anisotropy, Acta Mater., 212 (2021) 116876. https://doi.org/10.1016/j.actamat.2021.116876.

[36] S. Holland, X. Wang, J. Chen, W. Cai, F. Yan, L. Li, Multiscale characterization of microstructures and mechanical properties of Inconel 718 fabricated by selective laser melting, J. Alloys Compd., 784 (2019) 182-194. https://doi.org/10.1016/j.jallcom.2018.12.380.

[37] P. Ninpetch, P. Chalermkarnnon, P. Kowitwarangkul, Multiphysics Simulation of Thermal-Fluid Behavior in Laser Powder Bed Fusion of H13 Steel: Influence of Layer Thickness and Energy Input, Met. Mater. Int., 29 (2023) 536-551. https://doi.org/10.1007/s12540-022-01239-z.